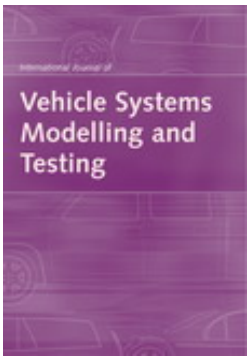

International Journal of Vehicle Systems Modelling and Testing

ISSN online: 1745-6444 - ISSN print: 1745-6436
https://www.inderscience.com/ijvsmt

Study on the influence of friction coefficient on the wheel-rail contact and rolling contact fatigue for the low-floor vehicle

Xue Li, Yuexin Wang, Kaiyun Wang, Gao Pu

DOI: 10.1504/IJVSMT.2025.10069248

Article History:

Received:	19 July 2024
Last revised:	19 September 2024
Accepted:	10 October 2024
Published online:	04 April 2025

Study on the influence of friction coefficient on the wheel-rail contact and rolling contact fatigue for the low-floor vehicle

Xue Li and Yuexin Wang

School of Mechanical Engineering,
Lanzhou Jiaotong University,
Lanzhou, 730070, China
Email: lzlix@mail.lzjtu.cn
Email: w18161278616@163.com

Kaiyun Wang*

State Key Laboratory of Rail Transit Vehicle System,
Southwest Jiaotong University,
Chengdu, 610031, China
Email: kywang@swjtu.edu.cn
*Corresponding author

Gao Pu

Chengdu Metro Operation Company,
Chengdu, 610074, China
Email: 1193164166@qq.com

Abstract: The wheel-rail friction coefficient (FC) is one of the critical parameters in the wheel-rail contact. This study focuses on the wheel-rail contact and rolling contact fatigue for the low-floor vehicle under the different FC. Firstly, the dynamic model of the low-floor vehicle is developed. Then, the area of contact patch, tangential stress, creep force, and normal force as the important indicators are investigated. Finally, based on the Shakedown Diagram and Dang-Van criterion, the rolling contact fatigue of traditional wheelset (TW) and independently rotating wheel (IRW) is studied. The results show that the superficial fatigue index of TW is always lower than that of IRW as the radius of the curve increases. The accumulated fatigue damage is more severe in the FC range of 0.15–0.25, where the accumulated fatigue damage of TW and IRW is increased by 0.0158 and 0.0311, respectively.

Keywords: vehicle system dynamics; low-floor vehicle; friction coefficient; rolling contact fatigue; wheel-rail contact.

Reference to this paper should be made as follows: Li, X., Wang, Y., Wang, K. and Pu, G. (2025) 'Study on the influence of friction coefficient on the wheel-rail contact and rolling contact fatigue for the low-floor vehicle', *Int. J. Vehicle Systems Modelling and Testing*, Vol. 19, No. 1, pp.74–89.

Biographical notes: Xue Li received her Master's degree in Lanzhou Jiaotong University, Lanzhou, China, in 2003. She co-hosted two National Natural Science Foundation projects, participated in one National Natural Science Foundation project and her major research fields include vehicle system dynamics analysis and vehicle equipment status monitoring and fault diagnosis.

Yuexin Wang received his Bachelor's degree in Chengdu Technological University, Chengdu, China, in 2022. He is currently pursuing the Master's degree in Vehicle Engineering. His major research field is vehicle system dynamics analysis.

Kaiyun Wang received his PhD in State Key Laboratory of Rail Transit Vehicle System, Southwest Jiaotong University, Chengdu, China, in 2013. He presided over four projects of the National Natural Science Foundation of China and published over 160 papers up to now. He received two National Scientific and Technological Progress Award.

Gao Pu received his Bachelor's degree in Lanzhou Jiaotong University, Lanzhou, China, in 1997. He is currently working in Chengdu Metro Operation Company, engaged in vehicle technology management.

1 Introduction

With the increasing running speed of urban rail transit and the complexity of the environment, fatigue damage and wheel-rail contact problems are becoming increasingly severe. The friction coefficient (FC) is one of the most critical parameters in the wheel-rail contact problem. The high friction-coefficient will affect the wheel-rail contact, and accelerate the crack propagation (Xiao et al., 2016). Therefore, studying the influence of FC on the wheel-rail contact and accumulated damage is of great significance for increasing the service life of wheels.

Gao et al. (2019) investigated the impact of different rail-cant on the wheel-rail contact of vehicle by spatial contact geometry algorithm. Zou et al. (2018) analysed the influence of wheel diameter difference on contact relationship for braking and sliding. Literature (Lu et al., 2017; Polach, 2016; Kaiser et al., 2020) explored the effects of wear and structural deformation on wheel-rail geometric contact parameters. Made et al. (2011) explored the influence of curve passing speed and vehicle weight on wheel-rail contact. Lei and Wang (2020) studied the wheel-rail interaction under the different wavelengths. Malvezzi et al. (2013) explored the relationship between adhesion coefficient and running speed. And they used neural network procedure to identify adhesion coefficient. In the above researches, the influence of different factors on wheel-rail contact has been studied. However, the influence of FC on the wheel-rail contact on different segments of same curved line still needs to be supplemented.

Xiao et al. (2016) found that wheels were mainly fatigue damage under the FC less than 0.2, while wheels were mainly wear damage more than 0.2. He et al. (2014) investigated the rolling contact fatigue under different curvature radii. Yang et al. (2021) found that the defects of the railroad sleeper greatly exacerbated the wheel-rail force, but it seldom affected distribution of fatigue damage. Wang et al. (2021) pointed out that the wheel diameter difference leads to asymmetrical tread wear, and increases the wheelset lateral-movement, resulting in expansion of fatigue area. Liu et al. (2022) studied the

effect of low adhesion at wheel-rail interface on the rolling contact fatigue of wheels. Liang et al. (2022) found that rail corrugation with longer-wavelength has a smaller impact on fatigue damage of wheels. Several authors (Taraf et al., 2010; Alarcón et al., 2016; Wang et al., 2010; Lin et al., 2015) studied the relationship between dynamic response, wear rate, fatigue damage, and wheel-rail FC. Eadie et al. (2008) pointed out that fatigue damage of wheel occurs because of high friction between the wheel and rail. Dirk and Enblom (2011) studied the influence of wear profiles and stiffness of primary suspension on rolling contact fatigue of wheels by Archard model and the damage function. de Paula Pacheco et al. (2023) applied the NSGA-II to optimise the wheel profiles, and predicted the service life of wheels. A lot of researches use Shakedown Diagram to study the fatigue damage of wheels. However, the Shakedown Diagram cannot predict the distribution of fatigue damage to the wheels and the fatigue life. Besides, the difference between the rolling contact fatigue of low-floor vehicle' TW and IRW is not studied deeply enough.

This paper aims to analyse the influence of FC on the wheel-rail interaction and the difference between rolling contact fatigue of low floor vehicle's TW and IRW. For this purpose, a low-floor vehicle dynamics model is developed, and the correctness of the dynamics model is verified based on field tests in Section 2. In Section 3, the simulation analyses of the wheel-rail interaction under the different FCs are carried out. In Section 4, the Shakedown Diagram and Dang-Van criterion are utilised to study the rolling contact fatigue. Lastly, some conclusions are drawn in Section 5.

2 Establishing the low-floor vehicle model

2.1 Vehicle system motion equation

To reflect the vibration performance of the vehicle as realistically as possible, the six degrees of freedom of vehicle body, bogie frame and wheelset are considered (Sun et al., 2020), the differential equation of vehicle dynamics as follows

$$M\ddot{X} + C\dot{X} + KX = F \tag{1}$$

where M, C, K are respectively the mass, damping, and stiffness matrices. $\ddot{X}$, $\dot{X}$, X are respectively the acceleration, velocity and displacement matrices. F is the load matrix.

2.2 Wheel-rail contact model

Wang et al. (2022) investigated the advantages of Kik-Piotrowski, Stripes, and Analyn contact models. They found that the accuracy of Kik-Piotrowski model is slightly higher than that of Analyse model, and the Stripes model is relatively the worst on the curve segment. Furthermore, Kik-Piotrowski model has the shortest calculation time, 0.25% of Contact model under the same conditions. Moreover, the calculation time required for Stripes and Analyse model is larger than that for Kik-Piotrowski model. Li (2020) pointed out that the calculation accuracy of the Kik-Piotrowski model is close to that of the Analyse model, and there is no local negative curvature problem in Kik-Piotrowski model, which can solve the contact problem that Analyse model cannot solve. Tao et al. (2016) found that the ratio of wear depth of Contact, Hertz, Kik-Piotrowski, Stripes and Analyn models is 1 : 0.82 : 0.92 : 0.82 : 0.75. The prediction results of the Kik-

Piotrowski model are more accurate. Sun et al. (2018) proved that the use of Kik-Piotrowski can well simulate the multi-point contact and non-Hertz contact behaviour, and the result is closer to that of Contact model.

Hence, the Kik-Piotrowski model is used in the subsequent simulation analysis. In wheel-rail contact relationship, the local coordinate system is defined with contact point as the coordinate origin. x is longitudinal direction, and the positive direction is the rolling forward direction of wheel. y represents the lateral direction, determined by the right-hand rule. The method in normal contact problem assumes that the two objects can penetrate each other. In reality, what occurs when the wheel contacts with the rail is the elastic deformation of the surface materials. The actual area will inevitably be smaller than the penetration area. Therefore, empirical coefficient ($\varepsilon = 0.55$) and the permeability are used to determine the contact area, and that distribution of compressive stresses should be consistent with the longitudinal contact boundary. The longitudinal contact boundary $a(y)$ and normal contact stress distribution $p(x, y)$ are as follows

$$a(y) \approx \sqrt{2R[\varepsilon\delta - f(y)]} \tag{2}$$

$$p(x, y) = \frac{P0}{a(0)} \times a(y) \times \sqrt{1 - \frac{x}{a(y)}} \tag{3}$$

where $f(y)$ is the normal clearance along the lateral direction in vicinity of the contact point. δ is the permeability. R is the radius of the wheel. And $P0$ is the normal contact stress at the contact origin.

Kalker simplified theory as follows is utilised to solve the tangential problem.

$$L\frac{\partial p_x}{\partial x} = -\xi_x + \varphi y + s_x \tag{4}$$

$$L\frac{\partial p_y}{\partial y} = -\xi_y + \varphi x + s_y \tag{5}$$

where L is the flexibility coefficient. p_x, p_y are respectively the longitudinal and lateral creep forces. s_x, s_y are respectively the velocity of creep. ξ_x, ξ_y, φ are respectively the longitudinal, lateral and spin creepages.

2.3 Dynamics model of vehicle

Figure 1 illustrates the dynamics model of the six-module low-floor vehicle. The model includes four motor vehicle subsystems, two trailer vehicle subsystems and the track subsystem. The vehicle body, frame, and wheels are represented as rigid bodies. The wheels are linked with the frame by primary suspensions; while the secondary suspensions, mainly air spring and damper, couple the bogie to the car body. The dynamics software UM (Universal Mechanism) is utilised to establish a low-floor vehicle dynamics model (see Figure 2). In modelling process, the suspension device is replaced by different forms of force elements. The motor vehicle model adopts the TW, and the trailer vehicle adopts the IRW. The connection between the motors and the trailer vehicles relies on the top linkage and the bottom articulation. The connection between the two modules relies on a buffer coupler. Table 1 shows the parameters of the established dynamics model of low-floor vehicle.

Figure 1 Topology diagram of vehicle dynamics model: (a) side view of vehicle; (b) end view of motor vehicle and (c) end view of trailer vehicle (see online version for colours)

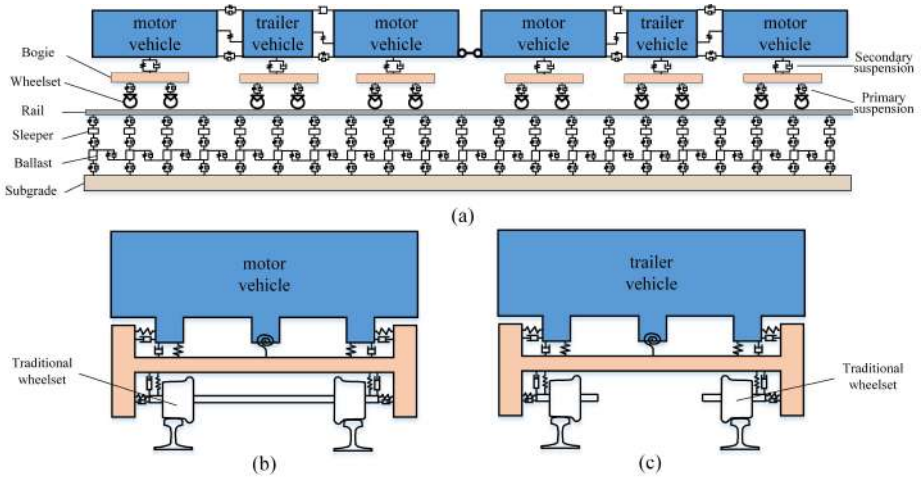

Figure 2 Vehicle system dynamics model in UM (see online version for colours)

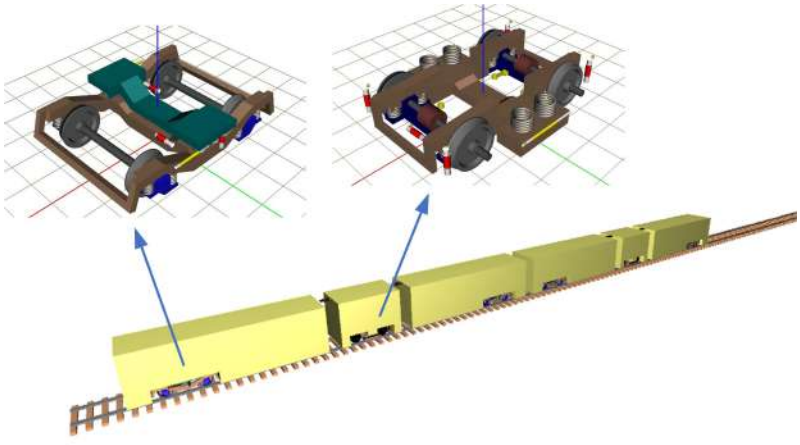

Table 1 Parameters of the low-floor vehicle

Parameter	*Unit*	*Motor car*	*Trailer*
Wheelset mass	kg	1500	750 (single wheel)
Frame mass	kg	2970	4224
Vehicle body mass	t	9	3.3
Wheelbase	m	1.85	1.85
Frame's moment of inertia in roll	$kg{\cdot}m^2$	1973	2084
Frame's moment of inertia in pitch	$kg{\cdot}m^2$	1876	1710
Frame's moment of inertia in yaw	$kg{\cdot}m^2$	3735	3635
Nominal rolling circle diameter	m	0.66	0.66

2.4 Validation of model

As shown in Figure 3(a) is the field test of vibration response for the low-floor vehicle.

To measure the acceleration signals of the low-floor vehicle, some acceleration sensors are utilised to measure the accelerations at some important locations on the field test. Here, two types of acceleration sensors are utilised: one has a sensitivity of 50.404 with a test range of 0–100 *g*, while the other has a sensitivity of 101.828 with a test range of 0–50 *g*. Measuring points nos. 1 and 2 respectively are each axle box and bogie frame directly above axle box (Figure 3(b) and (c)). Firstly, the block with threaded holes is pasted onto the measuring points during measurement. Then, the acceleration sensors with external threads are screwed into the block. Finally, the other end of the acceleration sensor is connected to the acquisition instrument. Due to the requirement of uninterrupted power supply for data collection, the acquisition instrument is installed in the carriage (Figure 3(d)). Meanwhile, the acquisition instrument is connected to a laptop through network cables, and the test data is gathered by the software package COINV DASP in the laptop.

Figure 3 Data acquisition system (see online version for colours)

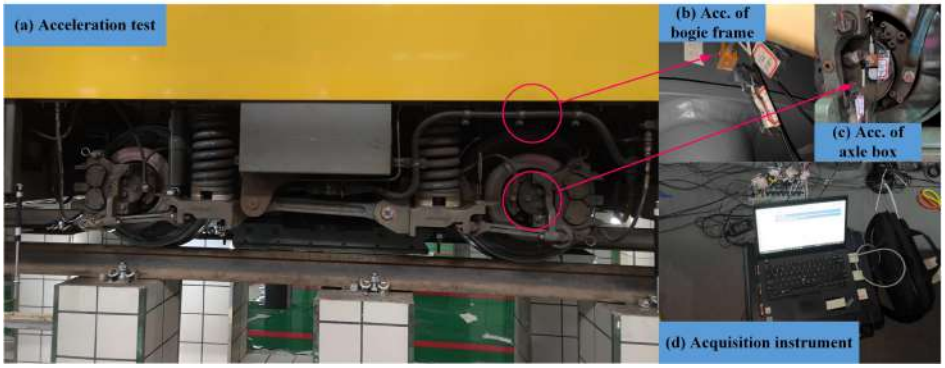

The dynamics model of the low-floor vehicle is utilised to calculate the vibration acceleration under the same running conditions. The results are compared with measured data on field tests to validate the model's reliability and ensure subsequent simulations' accuracy as shown in Figure 4. Notably, there is a slight difference between the simulation and test results. One important reason is that the electric motor was not considered in the dynamics model, but in reality, the power is provided by the electric motor and transmitted through the gearbox. During this process, the vibration generated by the traction system will be collected by acceleration sensors. Moreover, in the simulation analysis, the new wheels are used in the dynamics model, but on the low-floor vehicle under experiment, there will be some wear on the wheels during continuous running. Nevertheless, the similar variation and the slight difference between maximum values suggest that the dynamics model can be used for simulation calculations.

Figure 4 Verification of vehicle dynamics model: acceleration of axle box (a) and bogie frame (b) (see online version for colours)

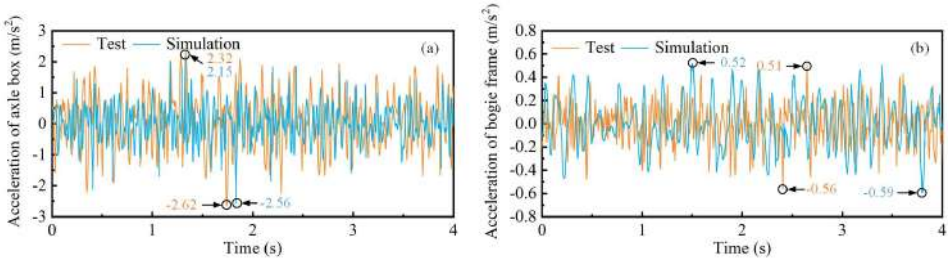

3 Wheel-rail contact

3.1 Dynamic contact points

It is generally believed that the more concentrated the wheel-rail contact location is, the better the running stability will be (Ma et al., 2018). The wheel-rail dynamic contact position under the 0.1–0.3 FC is studied on a straight line. Figure 5(a) shows the dynamic contact point position under the different FCs. The lateral distribution of dynamic contact points as follows can characterise the running stability of vehicle to a certain extent.

$$b_w = 2\sigma \tag{6}$$

where σ is the standard deviation of contact position.

Figure 5(b) illustrates the root mean square and lateral distribution of dynamic contact point. Obviously, as the FC increases, root mean square and lateral distribution width gradually increase, which means that the running stability of the vehicle decreases. Furthermore, as FC increases from 0.15 to 0.2, the root mean square and lateral distribution width reach the maximum increment of 0.8% and 2.7%, respectively.

Figure 5 Dynamic contact position of wheels under different FCs: (a) time-range curve of the wheel dynamic contact point position and (b) root mean square and lateral distribution width (see online version for colours)

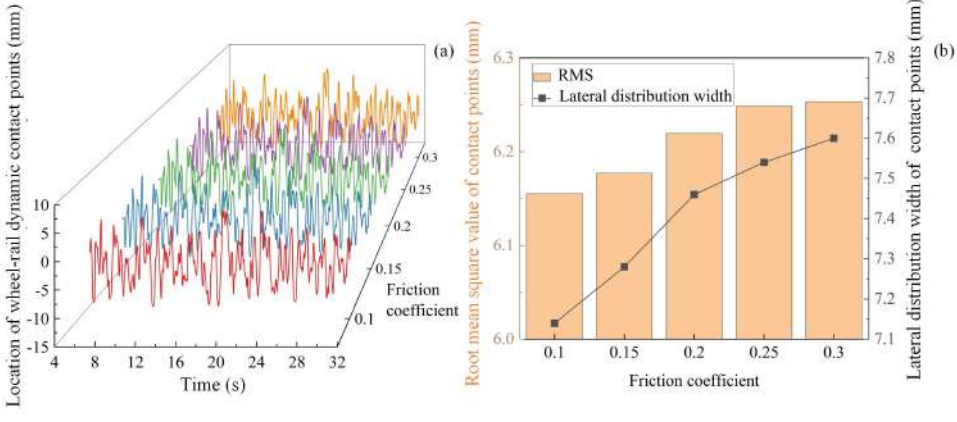

3.2 Dynamic contact performance between wheel and rail

The rail was simulated with CN 60 rail and LM worn-profile tread was applied to wheel profile. Considering the running environment of low-floor vehicle, the running speed is 40 km/h, and the superelevation is 0.095 m. The parameters of curve line are shown in Figure 6. The 500 m rail irregularity (see Figure 7) is applied to the established dynamics model of the low-floor vehicle.

Figure 6 Schematic diagram of curved line (see online version for colours)

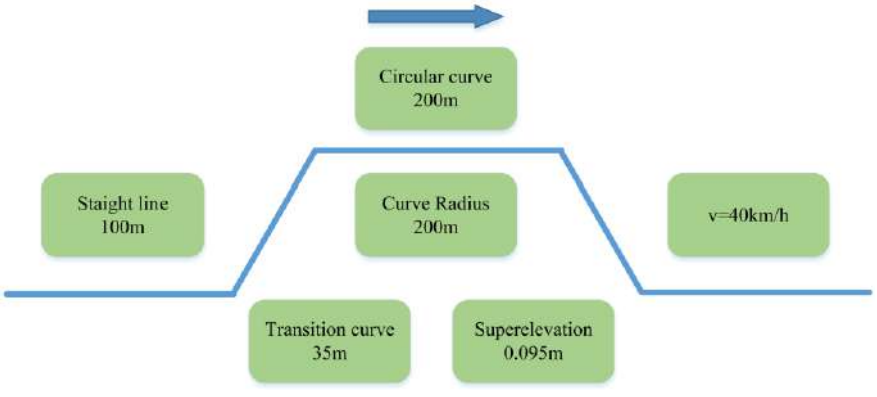

Figure 7 Rail irregularity: (a) vertical irregularities and (b) horizontal irregularities (see online version for colours)

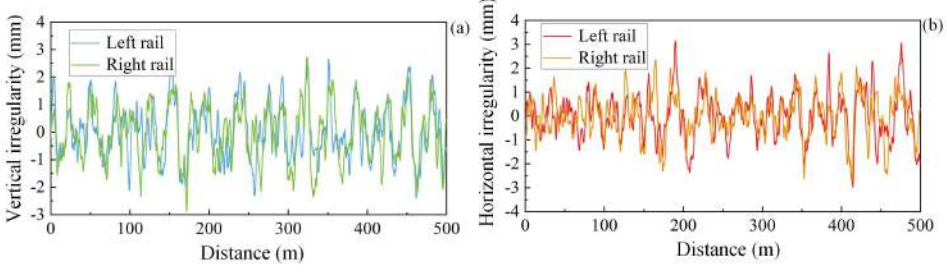

Figures 8 and 9 show the contact patches at the midpoint of front straight line segment and circular curve segment, respectively. It can be clearly seen that there is almost no change in the profile and area of contact patch at the two locations. There is a certain creep area in the contact patch in the straight line segment under the FC of 0.1. However, with the increasing FC, the area of creep declines, and the adhesion area escalates accordingly. In contrast, the large deviation between the centre of the wheel and track in the curved segment results in only a creep area within the contact patch. In addition, the tangential stress is very little affected by the FC on the straight line segment but significantly affected on the curved segment.

Figure 8 Contact patch at the midpoint of the front straight line segment: (a) $u = 0.1$; (b) $u = 0.15$; (c) $u = 0.2$; (d) $u = 0.25$ and (e) $u = 0.3$

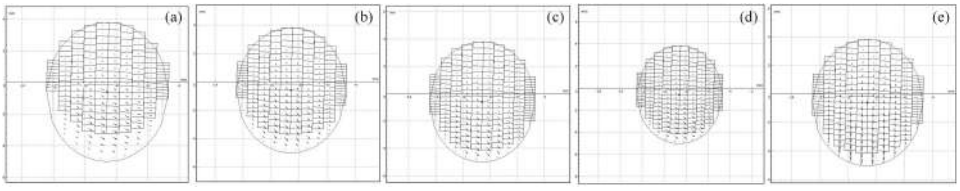

Figure 9 Contact patch at the midpoint of the circular curve segment: (a) $u = 0.1$; (b) $u = 0.15$; (c) $u = 0.2$; (d) $u = 0.25$ and (e) $u = 0.3$

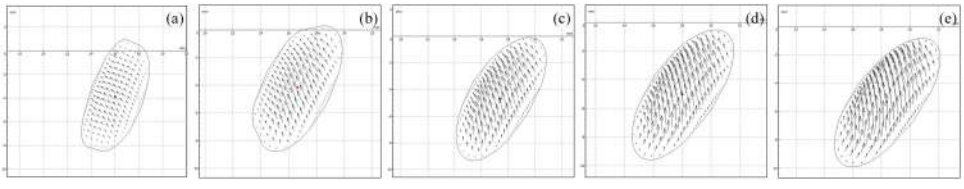

Figure 10 The variation of indicators under different the FC in each segment: (a) lateral creep force; (b) longitudinal creep force; (c) area of contact patch and (d) normal force (see online version for colours)

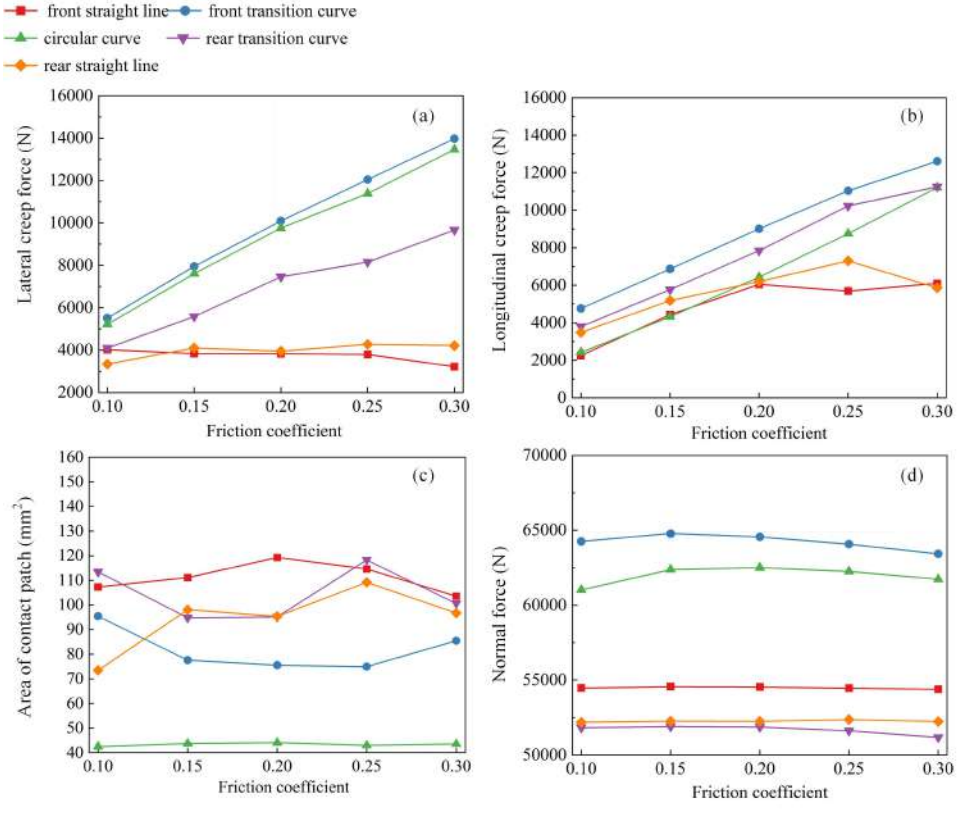

However, the contact patch in Figures 8 and 9 cannot intuitively reflect the creep force and normal force. Therefore, the complete curve crossing simulation is conducted. The route is divided into five segments. Then, the variation of each indicator in each segment as studied is presented in Figure 10.

Figure 10(a) reflects the variation of lateral creep force. As can be seen in the results that in the front and rear straight line segment, the lateral creep force hardly changes with the varying FC, fluctuating between 3–4 kN; whereas in the transition curve and circular curve segments, the lateral creep force is positively correlated with FC. The peak lateral creep forces approach 13.97 kN (front transition curve), 13.46 kN (circular curve), and 9.67 kN (rear transition curve) under the FC of 0.3, 153.6%, 158.1%, and 136.3% larger than those under the FC of 0.1, respectively.

Figure 10(b) illustrates the variation of longitudinal creep force. Obviously, the tendency of longitudinal creep force is similar with that of later creep force. The peak longitudinal creep forces approach 12.61 kN (front transition curve), 11.21 kN (circular curve), and 11.25 kN (rear transition curve) under the FC of 0.3, 164.7%, 363%, and 196.5% larger than those under the FC of 0.1, respectively.

Figure 10(c) displays the variation of contact patch area. It is worth mentioning that on the circular curve segment, the area of contact patch varies less under the varying FC, fluctuating within the range of 42–44 mm^2. Additionally, the contact patch area on the other four segments shows wide range of fluctuation.

Figure 10(d) displays the variation of normal force. When the FC increases by 0.2, the change trend of the normal force is slight in the front and rear straight line segment, increased by only 0.15%. Similarly, in the transition curve and circular curve segments, the normal force shows little sensitivity to changes in the FC.

4 Rolling contact fatigue of wheels

The Shakedown Diagram (Figure 11) is commonly applied to predict RCF (rolling contact fatigue) of wheels. This map is divided into plastic stability zone, elastic stability zone, elastic state zone and ratchet effect zone. Ekberg et al. (2002) proposed the superficial fatigue index (FI_s) expressed by equations (7) and (8), based on the shakedown diagram. FI_s represents horizontal distance between the contact point and ratchet effect curve, which reflects the difficulty of the occurrence of fatigue damage.

$$FI_S = \mu - \frac{2\pi abk}{3F_n} \tag{7}$$

$$\mu = \frac{\sqrt{T_x^2 + T_y^2}}{F_n} \tag{8}$$

where T_x, T_y are respectively the longitudinal and lateral force; a, b are respectively the short and long half shafts of contact patch; k is taken as 303 MPa here and is the shear yield strength; F_n is the normal force.

Figure 11 Shakedown diagram (see online version for colours)

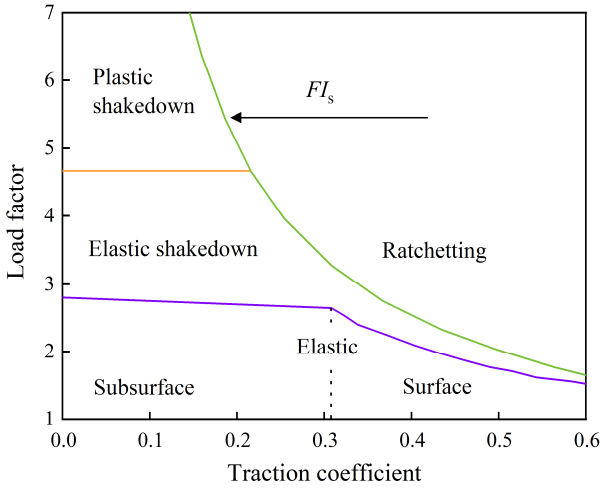

Since the low-floor motor vehicles adopt TW while the trailer vehicles adopt IRW, the performance of these two types of wheels varies when running on different tracks. Based on the service conditions, four track conditions are set in Table 2. The effect of FC on the fatigue damage of the wheels is studied separately.

Figure 12 displays the superficial fatigue index of two types of wheels on the R200m curve. It can be known that the superficial fatigue index is positively correlated with FC. The superficial fatigue indices of two wheels approach the peak values of 0.271 and 0.266 under the FC of 0.3, 262.7% and 251.3% larger than that under the FC of 0.1.

Figure 12 Time history curves of two types of wheel superficial fatigue index under the different FC: (a) TW and (b) IRW (see online version for colours)

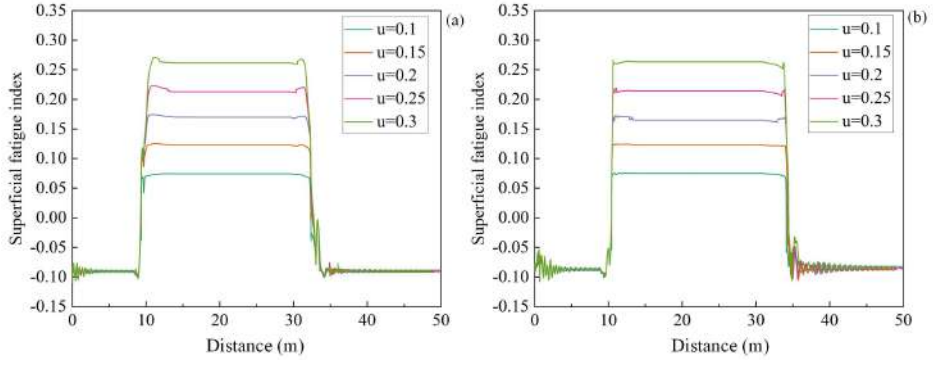

Furthermore, the superficial fatigue index is lower than 0 on the straight line. Therefore, it is difficult for fatigue damage to occur on the wheels (Silva e Silva et al., 2023). But on the transition curve and circular curve segment, the creep force is larger, and the area of contact patch is lower. Consequently, the superficial fatigue index increases dramatically and reaches the peak value, when vehicle enters transition curve segment, resulting in the increased probability of contact fatigue.

Table 2 Line operating condition settings

Conditions	*Track* (m)	*Velocity* (km/h)	*Superelevation* (m)
1	Straight line	60	–
2	R600	50	0.05
3	R200	40	0.095
4	R50	25	0.145

Figure 13 depicts the superficial fatigue index under the different FCs on the four track conditions. For the IRW, the superficial fatigue index is minimally affected by curve radius, as the curve radius changes from R600 to R50, the range of the superficial fatigue index is only 0.0072, with an increase of 2.7%. But for TW, the superficial fatigue index is increased by 35.3%. The superficial fatigue index is positively correlated with FC on the R50 and R200 curves. The rolling contact fatigue of TW is lower than that of IRW on the R600 curve. When the FC increases by 0.2, the superficial fatigue index of TW is increased by 0.137, 71.4% of that of IRW. Moreover, the superficial fatigue index of TW is always lower than that of IRW as the radius of the curve increases.

Figure 13 The superficial fatigue index of two types wheels under the different running conditions (see online version for colours)

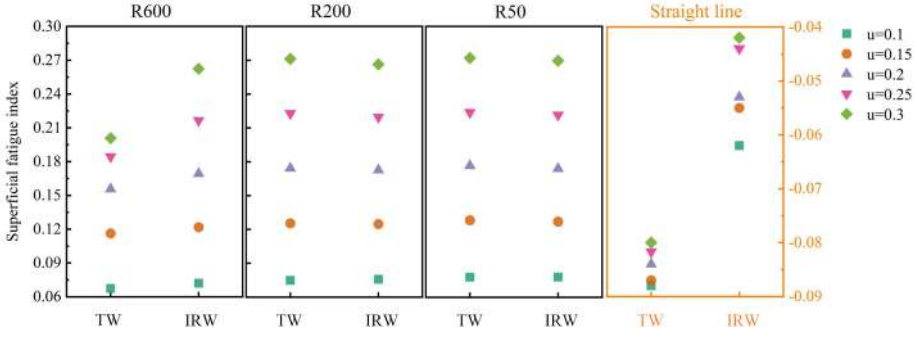

The shakedown diagram calculates the fatigue damage from a probabilistic perspective. However, the shakedown diagram cannot predict the accumulated damage of the wheel and the damage distribution. Therefore, the fatigue damage of the wheel is analysed by UM-RCF module and Dang Van criterion.

The Dang-Van criterion (Ekberg, 1996) is represented by two inequalities

$$\tau_{EQ1} = \tau_a(t) + \alpha_{DV}\sigma_h(t) > \tau_e \tag{9}$$

$$\tau_{EQ2} = \tau_a(t) - \alpha_{DV}\sigma_h(t) < -\tau_e \tag{10}$$

where $\tau_a(t)$ is the time-dependent value of the shear stress. $\sigma_h(t)$ is the time-dependent value of the hydrostatic stress. τ_e is the material parameter. α_{DV} is the Dang Van coefficient, equal to the tangent of the slope angle of the cyclic fatigue diagram. The criterion is numerically equal to the length of the segment OC cut off by the line parallel to the inclined line of the diagram passing through point A with the coordinates $\sigma_h(t)$ and $\tau_a(t)$ presented in Figure 14. The inclined straight line passing through the point D

cuts off a short segment on the $\tau_a(t)$ axis. If the line intersects the $\tau_a(t)$ axis at the point with the negative value of the criterion, the criterion is 0. If only the absolute value of the shear stress $\tau_a(t)$ is taken into consideration in calculations, then only the upper part of the diagram can be used. The Dang-Van criterion can be represented in equation (11).

$$\tau_{DV} = \left|\tau_a(t)\right| + \alpha_{DV}\sigma_h(t) \tag{11}$$

The value of the coefficient in this paper is 0.38 (Bernasconi et al., 2005).

Figure 14 Determination of safety factor using fatigue diagram

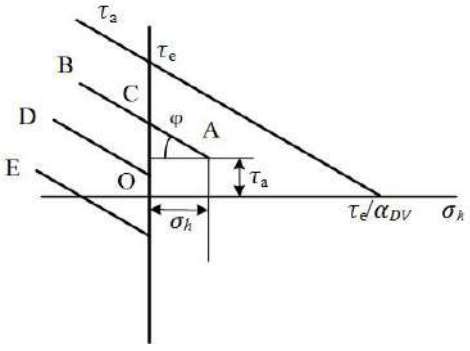

Figure 15 shows the distribution of two types wheels after the vehicle running 20,000 km under the FC of 0.3. The x-axis origin in the diagram represents the nominal rolling circle of the wheels. It is notable that the maximum accumulated damage of TW is distributed near the nominal rolling circle. However, it is difficult to form effective torque due to IRW's almost zero longitudinal creep force. As a result, under the excitation of the rail irregularity, the automatic centring ability of IRW is weak (Li et al., 2019), which generates wear near the wheel flange. Therefore, there is equally large accumulated damage near the wheel flange.

Figure 15 Fatigue damage of two types wheels under the FC of 0.3: (a) TW and (b) IRW (see online version for colours)

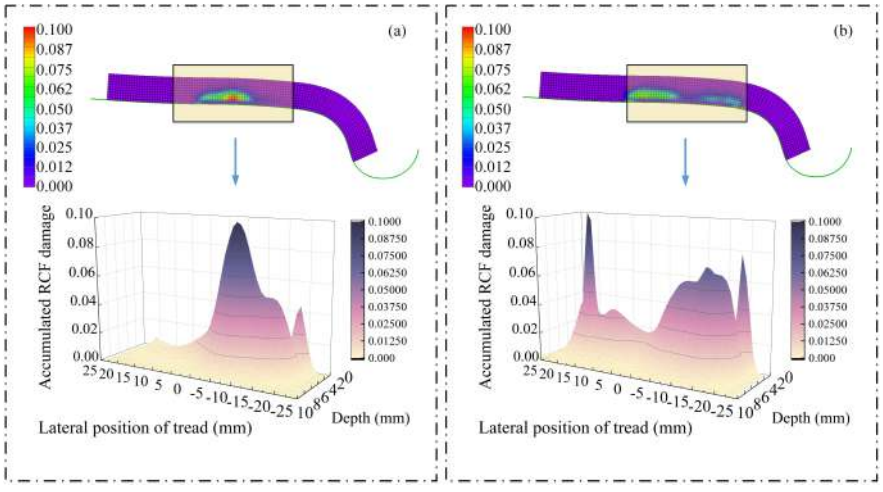

Figure 16 displays the peak accumulated damage of two wheels under the different FC. The simulation results indicate that the accumulated damage is positively correlated with FC. The accumulated damage is more severe in range of 0.15–0.25, where the accumulated fatigue of TW and IRW is increased by 0.0158 and 0.0311 respectively. Besides, the increase in fatigue damage is more significant for IRW. When the FC increases by 0.2, the fatigue damage of the TW is increased by 20.8%; while for IRW, it is increased by 37.6%.

Figure 16 Peak values of fatigue damage for two types of wheels for different FC conditions (see online version for colours)

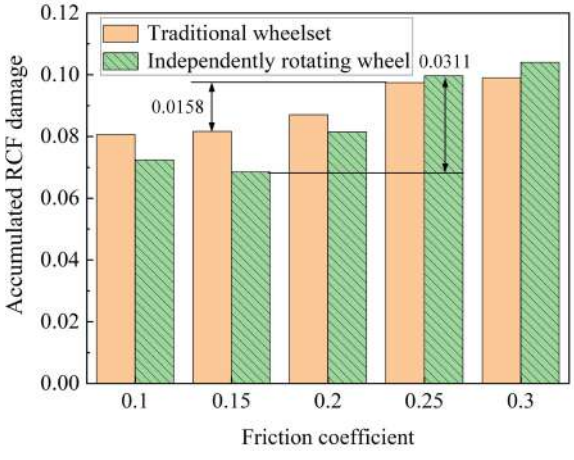

5 Conclusions

A dynamic model of low-floor vehicle is established using the theory of vehicle-track coupled dynamics in this paper. The effect of the FC on wheel-rail contact and rolling contact fatigue of wheels is studied, and the difference in fatigue damage between TW and IRW is specifically compared. The analysis results can provide useful references for wheel-rail lubrication of low-floor vehicles and increasing the service life of wheels. Main conclusions can be drawn as follows:

1 On the straight line, the creep area of the contact patch declines and the adhesion area increases with the increasing FC. On the curved segment, the creep forces are positively correlated with the FC, but the normal force fluctuates less under the different FC.

2 The superficial fatigue index of TW is increased by 0.137 on the R = 600 m curve, 71.4% of that of IRW. Moreover, the superficial fatigue index of TW is always lower than that of IRW as the radius of the curve increases.

3 The weak automatic centring ability of IRW could result in large accumulated damage near the wheel flange. The accumulated fatigue damage is more severe within the FC range of 0.15–0.25.

Acknowledgements

This research was supported by the National Natural Science Foundation of China (61863021), and the Special Funds for Guiding Local Scientific and Technological Development by the Central Government (22ZY1QA005).

References

Alarcón, G.I., Burgelman, N., Meza, J.M., Toro, A. and Li, Z. (2016) 'Power dissipation modeling in wheel/rail contact: effect of FC and profile quality', *Wear*, Vols. 366–367, pp.217–224.

Bernasconi, A., Davoli, P., Filippini, M. and Foletti, S. (2005) 'An integrated approach to rolling contact subsurface fatigue assessment of railway wheels', *Wear*, Vol. 258, pp.973–980.

de Paula Pacheco, P.A., Endlich, C.S., Vieira, K.L.S., Reis, T., dos Santos, G.F.M. and dos Santos Júnior, A.A. (2023) 'Optimization of heavy haul railway wheel profile based on rolling contact fatigue and wear performance', *Wear*, Vol. 522 p.204704.

Dirk, B. and Enblom, R. (2011) 'Prediction model for wheel profile wear and rolling cantact fatigue', *Wear*, Vol. 271, pp.210–217.

Eadie, D.T., Elvidge, D., Oldknow, K., Stock, R., Pointner, P., Kalousek, J. and Klauser, P. (2008) 'The effects of top of rail friction modifier on wear and rolling contact fatigue: full-scale-rail-wheel test rig evaluation, analysis and modelling', *Wear*, Vol. 265, No. 9, pp.1222–1230.

Ekberg, A. (1996) 'Rolling contact fatigue of railway wheels-computer modelling and in-field data', *Proc. of the 2nd Mini Conf. Contact Mechanics and Wear of Rail-Wheel Systems*, Budapest, pp.154–163.

Ekberg, A., Kabo, E. and Andersson, H. (2002) 'An engineering model for prediction of rolling contact fatigue of railway wheel', *Fatigue and Fracture of Engineering Materials and Structures*, Vol. 25, No. 10, pp.899–909.

Gao, Y., Shi, J. and Li, K.F. (2019) 'Influence of rail cant on wheel-rail contact characteristics of operating metro', *Journal of Beijing Jiaotong University*, Vol. 43, No. 6, pp.25–33.

He, C.G., Zhou, G.Y., Wang, J., Wen, G., Wang, W.J. and Liu Q.Y. (2014) 'Effect of curve radius of rail on rolling contact fatigue properties of wheel steel', *Tribology*, Vol. 34, No. 3, pp.256–261.

Kaiser, I., Poll, G. and Vinolas, J. (2020) 'Modelling the impact of structural flexibility of wheelsets and rails on the wheel-rail contact and the wear', *Wear*, Vol. 504, p.203445.

Lei, Z.Y. and Wang, Z.Q. (2020) 'Contact and creep characteristics of wheel–rail system under harmonic corrugation excitation', *Journal of Vibration and Control*, Vol. 7, Nos. 17–18, pp.2069–2080.

Li, J.C., Ding, J.J. and Wu, P.P., Yang, Y. and Li, F. (2019) 'Analysis of dynamics and wheel wear of low floor vehicle based on different patterns', *Journal of Southwest JiaoTong University*, Vol. 54, No. 1, pp.14–22.

Li, Y.Y. (2020) *The Research on Wheel Wear Prediction of High-Speed Train*, Beijing Jiaotong University, Beijing.

Liang, H.Q., Li, W., Zhou, Z.J., Wen, Z.F., Li, S.G. and An, D. (2022) 'Investigation on rail corrugation grinding criterion based on coupled vehicle–track dynamics and rolling contact fatigue model', *Journal of Vibration and Control*, Vol. 8, Nos. 9–10, pp.1176–1186.

Lin, S.P., Takino, Y., Suda, Y., Hashimoto, M., Nakano, D., Tanimoto, A. and Kageyama, M. (2015) 'Study on dynamics of lightweight railway vehicle with different coefficients of friction in wet condition', *Dynamics of Vehicles on Roads and Tracks*, pp.1499–1504.

Liu, Y.F., Zhao, X.F., Li, Y., Wen, Z.F. and Zhao X. (2022) 'Effect of low adhesion between wheel and rail on wheel rolling contact fatigue of high-power ac locomotives', *Journal of the China Railway Society*, Vol. 44, No. 12, pp.22–29.

Lu, W.J., Tao, G.Q., Wang, P., Fu, Q.Y., Guan, Q.H. and Wen, Z.F. (2017) 'Influence of wheel wear on wheel rail contact behavior and dynamic performance of metro vehicle', *Engineering Mechanics*, Vol. 34, No. 8, pp.222–231.

Ma, X.C., Wang, P., Xu, J.M., Wang, J. and Hu, C.Y. (2018) 'Dynamic performance analysis of high speed vehicle based on LMA worn wheel matching with 60N rail', *China Railway Science*, Vol. 39, No. 1, pp.93–99.

Made, P., Bagus, B., Satryo, S.B., and Wiratmaja Puja, I.G.N. (2011) 'Effect of curving speed and mass of railway vehicle to the contact characteristic on curve track', *International Journal of Vehicle Systems Modelling and Testing*, Vol. 6, Nos. 3–4, pp.250–267.

Malvezzi, M., Pugi, L., Papini, S., Rindi, A. and Toni, P. (2013) 'Identification of a wheel. rail adhesion coefficient from experimental data during braking tests', *Proceedings of the Institution of Mechanical Engineers*, *Part F: Journal of Rail and Rapid Transit*, Vol. 227, No. 2, pp.128–139.

Polach, O. (2016) 'Wheel-rail contact geometry parameters in regard to vehicle behaviour and their alteration with wear', *Wear*, Vol. 366, pp.200–208.

Silva e Silva, J.V.R., Antoniolli, F.A., Endlich, C.S., Pires, A.C., Scandian, C. and dos Santos, G.F.M. (2023) 'Influence of wheel tread wear on rolling contact fatigue and on the dynamics of railway vehicles', *Wear*, Vol. 523, p.204735.

Sun, L.X., Li, X.F., Hu, X.Y., Chang, C.Y., Cheng, D. and Zhou, C.Y. (2020) 'Influence of wheel wear on wheel-rail contact relationship and vehicle dynamic performance of high-speed EMU', *China Railway Science*, Vol. 41, No. 6, pp.117–126.

Sun, Y., Zhu, S.Y. and Zhai, W.M. (2018) 'Influence of tread hollow-worn wheel on wheel-rail interaction', *Journal of Mechanical Engineering*, Vol. 54, No. 4, pp.109–116.

Tao, G.Q., Wen, Z.F., Zhao, X. and Jin, X.S. (2016) 'Effects of wheel–rail contact modelling on wheel wear simulation', *Wear*, Vols. 366–367, pp.146–156.

Taraf, M., Zahaf, E.H., Oussouaddi, O. and Zeghloul, A. (2010) 'Numerical analysis for predicting the rolling contact fatigue crack initiation in a railway wheel steel', *Tribology International*, Vol. 43, pp.585–593.

Wang, H.B., Ding, W.C., Song, Y.F., Li, G.F., Wu, B.H. and Wang, X.P. (2021) 'Analysis of the influence of wheel diameter difference on wheel tread wear and rolling contact fatigue', *Journal of Railway Science and Engineering*, Vol. 18, No. 5, pp.1277–1288.

Wang, J.X., Xiao, W. and Zhang, X.D. (2010) 'Effect of wheel-rail friction on rolling contact fatigue', *Advanced Materials Research*, Vols. 160–162, pp.1636–1640.

Wang, P., Zhou, J.Y., Wang, P.J., Chen, S. and An, B.Y. (2022) 'Comparative study of three non-Hertzian rolling contact models', *Journal of the China Railway Society*, Vol. 44, No. 1, pp.39–47.

Xiao, Q., Fang, J. and Wang, L. (2016) 'Influence of FC on wheel transient rolling contact fatigue of high speed train', *China Railway Science*, Vol. 37, No. 3, pp.68–74.

Xiao, Q., Huang, B.K., Yang, Y.H. and Chang, C. (2016) 'Research on the influence of FC on the wear of high-speed wheels and rails', *Journal of the China Railway Society*, Vol. 38, No. 4, pp.39–43.

Yang, F., Wei, Z.L., Sun, X.F., Shen, C. and Núñez, A. (2021) 'Wheel-rail rolling contact behavior induced by both rail surface irregularity and sleeper hanging defects on a high-speed railway line', *Engineering Failure Analysis*, Vol. 128, p.105604.

Zou, R., Ma, W. and Luo, S. (2018) 'Influence of the wheel diameter difference on the wheel/rail dynamic contact relationship of the heavy haul locomotive', *Australian Journal of Mechanical Engineering*, Vol. 16, No. 2, pp.1–11.